TU Delft

Delft University of Technology

The Near-Wake of Super-Critical Discrete Roughness Elements on Swept Wings

Zoppini, G.; Sequeira, A.D.; Michelis, Theodorus; Ragni, D.; Kotsonis, M.

DOI
10.2514/6.2023-2306

Publication date
2023

Document Version
Final published version

Published in
AIAA SciTech Forum 2023

Citation (APA)
Zoppini, G., Sequeira, A. D., Michelis, T., Ragni, D., & Kotsonis, M. (2023). The Near-Wake of Super-Critical Discrete Roughness Elements on Swept Wings. In *AIAA SciTech Forum 2023* Article AIAA 2023-2306 (AIAA SciTech Forum and Exposition, 2023). https://doi.org/10.2514/6.2023-2306

Important note
To cite this publication, please use the final published version (if applicable).
Please check the document version above.

Copyright
Other than for strictly personal use, it is not permitted to download, forward or distribute the text or part of it, without the consent of the author(s) and/or copyright holder(s), unless the work is under an open content license such as Creative Commons.

Takedown policy
Please contact us and provide details if you believe this document breaches copyrights.
We will remove access to the work immediately and investigate your claim.

This work is downloaded from Delft University of Technology.
For technical reasons the number of authors shown on this cover page is limited to a maximum of 10.

AIAA SciTech Forum
23-27 January 2023, National Harbor, MD & Online
AIAA SCITECH 2023 Forum

10.2514/6.2023-2306

The Near-Wake of Super-Critical Discrete Roughness Elements on Swept Wings

G. Zoppini*, A. Sequeira†, T. Michelis‡, D. Ragni§ and M. Kotsonis¶
Delft University of Technology, Delft, The Netherlands, 2629HS

The present work details the steady and unsteady flow topology in the vicinity of an array of periodically spaced super-critical (i.e. causing flow tripping) discrete roughness elements (DRE) applied in a swept wing boundary layer. The stationary flow field is acquired by means of high-magnification dual-pulse tomographic particle tracking velocimetry (3D-PTV), while the unsteady instabilities are investigated through high-resolution hot wire anemometry (HWA). The 3D-PTV time-averaged velocity fields, indicate that the near-element flow region is dominated by the alternation of high- and low-speed streaks. A high-speed region substitutes the wake development shortly downstream of the DRE location, due to the high-speed streaks merging. This initiates a region of strong unsteady fluctuations that expands in the spanwise and wall-normal directions, ultimately leading to the boundary layer transition to turbulence. The spectral content of the stationary flow structures is investigated through a spanwise spatial Fourier transform. The extracted spectra and instability amplitudes, indicate the presence of non-modal mechanisms in the near-element stationary wake region. Nonetheless, the temporal spectral analysis of the HWA velocity signal, identifies the presence of strongly tonal shedding mechanisms initiating and the unsteady instabilities the element vicinity. Their rapid downstream growth and evolution retains a fundamental role in the transitional process.

Downloaded by TU DELFT on January 24, 2023 | http://arc.aiaa.org | DOI: 10.2514/6.2023-2306

Nomenclature

α	=	Angle of attack, deg.	c	=	Leading edge orthogonal chord, m.
c_X	=	Streamwise chord, m.	d	=	Element diameter, mm.
δ_{99}	=	Boundary-layer displacement thickness, mm.	k	=	Element height, mm.
$\mathrm{Re_k}$	=	Roughness Reynolds number, $\frac{\lvert\mathbf{u}(k)\rvert k}{\nu}$.	Re_{c_X}	=	Reynolds number, $\frac{\overline{u}_\infty c_X}{\nu}$.
$\overline{u}_\infty$	=	Free-stream velocity, ms^{-1}.	λ	=	Roughness elements inter-spacing.
X, Y, Z	=	Tunnel-attached coordinate system.			
x, y, z	=	Wing-attached coordinate system.			

I. Introduction

The evolution and transitional process of swept wing boundary layers (BL) in low freestream turbulence environments, is typically dominated by the development of stationary crossflow instabilities (CFI) [1–4]. The instabilities onset conditions are determined by the receptivity process [5], which in the case of stationary CFI is highly sensitive to surface roughness [2]. In particular, numerous experimental and numerical works apply spanwise-periodic DRE arrays to investigate the development of stationary CFI, as they initiate a monochromatic spanwise-uniform instability mode [3, 6, 7]. To characterize the employed roughness configurations, a roughness-based Reynolds number is defined as $\mathrm{Re_k} = \frac{\lvert\mathbf{u}(k)\rvert \mathrm{k}}{\nu}$ [6, 8], where $\mathbf{u}(\mathrm{k})$ is the local BL velocity at the roughness element height k and ν is the kinematic viscosity. This geometrical parameter, proved successful for the characterization of the downstream influence of DRE on the flow field, discriminating between *critical* and *super-critical* forcing configurations. Specifically, forcing configurations leading to the onset of stationary CFI are considered *critical*. Instead, forcing configurations that trigger

*PhD Candidate, Section of Aerodynamics, Faculty of Aerospace Engineering, AIAA Student Member.
†MSc Student, Section of Aerodynamics, Faculty of Aerospace Engineering
‡Post-Doc Researcher, Section of Aerodynamics, Faculty of Aerospace Engineering
§Associate Professor, Section of Wind Energy, Faculty of Aerospace Engineering
¶Associate Professor, Section of Aerodynamics, Faculty of Aerospace Engineering

Copyright © 2023 by G. Zoppini, A. Sequeira, T. Michelis, D. Ragni, M. Kotsonis. Published by the American Institute of Aeronautics and Astronautics, Inc., with permission.

turbulence and initiate BL transition in the DRE vicinity, are defined as *super-critical*. Nonetheless, Re_k does not provide detailed information regarding the receptivity or transitional process. Additionally, despite their fundamental role for the onset and development of CFI, only few experimental and numerical studies focussed on the characterization of the near-element flow topology and the initial phases of receptivity. Within the experimental framework, this can be attributed to the large disparity of scales over which the phenomena of interest occur, posing severe challenges for modern flow measurement techniques. Furthermore, the possible presence of non-modal mechanisms [9–11] and the multitude of parameters involved (e.g. freestream turbulence, local pressure gradient), complicate the development of numerical tools capable of fully describing the near-element flow features and the successive CFI onset.

Among the few works characterizing the near-element flow topology, DNS investigations Kurz and Kloker [12] and Brynjell-Rahkola et al. [13], indicate that a complex vortical system develops around and aft of each element in a DRE array. Two pairs of counter-rotating horseshoe vortex systems form: an outer leg pair generated upstream of the DRE due to the roll-up of streamwise BL vorticity, and an inner pair that originates aft of the DRE due to the lift-up effect [14]. The flow features in the vicinity of the element are similar for both 2D and 3D boundary layers. However, the presence of the crossflow velocity component in the 3D boundary layer baseflow leads to an asymmetric downstream development of the re-circulation region and HSV legs. Specifically, the sense of rotation dictated by the crossflow velocity component is preferred, hence, only structures co-rotating with the crossflow are sustained by the baseflow [12]. Eventually, only one leg is retained within each of the two HSV pairs. For a critical Re_k, the retained structures are amplified, likely evolving into stationary CFI further downstream [11, 12]. A super-critical forcing, instead, induces a stronger recirculation region aft of each DRE, rapidly amplifying steady and unsteady disturbances initiated in the element's wake to non-linear levels [15, 16]. Such flow scenario, originates turbulent wedges or vortical structures in the DRE vicinity, which rapidly develop and drive the BL transition to turbulence [12, 13].

The reported DNS studies provided substantial insight into DRE near-element flow behaviour. Nonetheless, a full description of the steady and unsteady instabilities and mechanisms dominating the near-element flow, along with their relation to receptivity, remains an open subject. As the flow topology immediately aft of the DRE shares much between 2D and 3D scenarios, the near-element flow physics in 3D boundary layers may be partially inferred from the vast literature available on roughness receptivity in 2D boundary layers [9, 17–19]. Many studies investigating 2D boundary layers, reported the occurrence of transient instability growth [20] in the flow region immediately aft of the DRE (i.e. the near-wake). Transient growth, has been identified as a fundamental receptivity mechanism in the steady and unsteady development of the near-wake region in 2D boundary layer scenarios [9, 21]. Recent investigations conducted by the authors [10, 11] indicate that transient growth also characterizes the stationary near-wake flow evolution of critical DREs in 3D boundary layers. Nonetheless, while investigating the near-wake flow topology in 2D boundary layers, Ergin and White [22] outlined the occurrence of two competing mechanisms. On the one hand, the steady disturbances (i.e. the velocity streaks structures) tend to relax into a basic state, as shown by the initial decay of the corresponding disturbance energy. On the other hand, unsteady disturbances initiated in the element vicinity, tend to rapidly grow. The balance (or unbalance) between these two processes can either lead to the development of an inviscid instability mechanism, such as the CFI, or it can lead to the breakdown of the laminar streaks and the onset of turbulence. The latter scenario is typical of super-critical forcing cases, in which the enhanced recirculation region and shear-layers developing aft of the elements, lead to an explosive growth of unsteady fluctuations in the element vicinity.

Within the literature framework discussed beforehand, the present work aims at extending the near-element flow investigation, providing a detailed characterization of the flow topology along with pertinent receptivity and transitional mechanisms for a super-critical (i.e. tripping) roughness configuration in a 3D boundary layer. This includes the first comprehensive experimental investigation of the DRE near-element flow region, identifying the evolution of the dominant steady structures as well as competing unsteady mechanisms that lead to the onset of turbulence over the development of stationary CFI. These measurements are conducted through high-resolution dual-pulse tomographic particle tracking velocimetry (PTV) that allows for the acquisition of the full 3D stationary velocity field in the DRE vicinity. Fast Fourier (FFT) analysis on the time-averaged PTV velocity fields allows for determination of the spatial spectral content of the DRE wakes, along with the extraction of the stationary instability amplitudes and possible identification of non-modal mechanisms. Additionally, local hot wire anemometry (HWA) is performed to identify and temporally resolve regions of high unsteadiness in the near-element flow. This complements the stationary flow analysis, providing information regarding the time-frequency content of the unsteady velocity signal. The obtained temporal spectra, outline the presence of shedding mechanisms in the element vicinity, responsible for the unsteady instabilities onset and potentially driving the boundary layer transition to turbulence.

Downloaded by TU DELFT on January 24, 2023 | http://arc.aiaa.org | DOI: 10.2514/6.2023-2306

II. Methodology

A. Wind Tunnel, Swept Wing Model and Surface Roughness Configuration

The present work is based on experimental measurements conducted in an atmospheric closed return tunnel, featuring a low-speed and low-turbulence test section flow [23]. A constant-chord swept wing model (M3J, [23]), is measured throughout the current investigation. The wing model features a favorable pressure gradient, such that the natural (i.e. unperturbed) 3D boundary layer transitional process is dominated by stationary CFI [1, 2]. The acquisitions are preformed at a fixed angle of attack (α=-3.36°) and freestream Reynolds number (Re_{cx}=2.17×10^6). A steady and incompressible numerical BL solution, and the corresponding linear stability solution [LST, 24] are as well computed using an in-house developed routine [25].

Two coordinate reference systems are applied throughout the presented analysis: one is integral with the wind tunnel floor, with spatial components XYZ and velocity U,V,W; the second one is integral to the wing model, with z-axis and x-axis respectively aligned and orthogonal to the leading edge, spatial components xyz and velocity *u,v,w*.

Following previous investigations [6], a DRE array is applied on the wing surface with elements inter-spacing (i.e. the forced mode) corresponding to the most critical wavelength λ_1=8mm, as predicted by LST [25, 26]. The forcing configuration investigated throughout this work, features cylindrical DRE of nominal height k=0.4mm and diameter d=2mm. To gain better access to the experimental domain of interest, the array is applied at x/c=0.15 [10], where the unperturbed (i.e. no DRE applied) experimental BL thickness is $\delta_{99} \simeq$1.3mm. The measured forcing configuration can be described by the roughness Reynolds number, corresponding to Re_k=330. Previous investigations, showed that in the current set-up configurations featuring $Re_k \geq$200 behave super-critically [10]. Hence, the chosen configuration is expected to introduce near-element instabilities that rapidly grow and breakdown, causing transition in the element vicinity preventing the development of classical stationary CFI.

B. Measurement Techniques and Data Analysis

1. Infrared Thermography (IR)

Infrared (IR) thermographic imaging acquires the wing pressure-side surface temperature and its modifications due to external heat deposition [1, 3]. This method capitalizes on the Reynolds' analogy [27], associating the laminar (turbulent) flow regions, characterized by a lower (higher) convective heat transfer coefficient, to warmer (colder) regions of the thermal image.

In the current application, the IR acquisitions are performed with two Optris PI640 IR cameras: one camera is equipped with a wide angle lens, (focal length f=10.5 mm), and images the whole wing chord length with resolution 0.85mm/px; the second camera features a zoomed-in lens (f=18.7mm) and captures a small domain aligned with the leading edge and centred at x/c=0.20 with resolution 0.43mm/px. The wide-lens configuration provides a global overview of the developing BL flow, indicating whether turbulent transition occurs in the element vicinity. The zoomed-in configuration allows for the preliminary characterization of the near-element flow features.

During the acquisition, five external halogen lamps ($3 \times$ 400W and $2 \times$ 500W) actively heat the model surface, improving the thermal contrast between the laminar and turbulent BL region. Acquisitions are performed collecting 80 images at a frequency of 4Hz, averaging them to reduce the signal-to-noise ratio. The averaged images are then geometrically mapped to the XYZ Cartesian framework by applying an in-house calibration procedure [28].

2. Dual-Pulse Tomographic Particle Tracking Velocimetry (3D PTV)

High-magnification dual-pulse tomographic Particle Tracking Velocimetry [PTV, 29–31] is employed to incur the steady 3D velocity distribution in the DRE vicinity. The flow fields are acquired in the xyz reference frame. Throughout the following discussion, the wall-normal direction (y) is non-dimensionalised by the BL displacement thickness extracted at x/c=0.165 for Re_{cx}=2.17×10^6, hereafter defined $\overline{\delta}^*$=0.46mm. The measured domain is centred at x/c=0.165 and extends for x/c=0.025, y/$\overline{\delta}^*$=6 and z/λ_1=3.5.

A Quantel Evergreen Nd:YAG dual cavity laser optically accesses the domain through a plexiglass window cut on the test section floor. The laser beam is shaped in a 4mm thick sheet, parallel to the wing surface in the area of interest. The flow field is acquired by 4 sCMOS LaVision Imager cameras installed on the test section side with a tomographic aperture of approximately 45°. Each camera features a 200mm lens, a 2X teleconverter and a lens-tilt mechanism complying with the Scheimpflug condition. This optical arrangement results in a focal length of 400mm, with spatial

Downloaded by TU DELFT on January 24, 2023 | http://arc.aiaa.org | DOI: 10.2514/6.2023-2306

resolution of 67px/mm. To keep the particles in focus throughout the entire volume depth, $f_\#$ is set to 11. The flow is seeded by dispersing 0.5μm droplets of a water-glycol mixture in the tunnel flow.

The image acquisition is performed at 10Hz, collecting 4000 image pairs with time interval of 8μs (i.e. 10px particle displacement in the freestream). The tomographic imaging system is calibrated through a double-layer target and through the volume self-calibration procedure [30, 32], resulting in a calibration uncertainty of $\simeq$0.04 px. The image pairs are processed in LaVision DaVis 10 through a shake-the-box, dual-pulse algorithm [31] identifying the particle trajectories within the acquired 3D volume. An in-house developed Matlab routine performs the binning and conversion to a Cartesian grid of the particle tracks, resulting in a vector spacing of 0.25mm in the xz plane and 0.04mm along y.

Time-averaged $(\overline{u}, \overline{v}, \overline{w})$ and standard deviation (u', v', w') velocity fields are obtained for all three velocity components in the xyz domain. The main data processing techniques are hereafter described as applied to $\overline{u}$, as the treatment of $\overline{v}$ and $\overline{w}$ follows a comparable procedure. By averaging the $\overline{u}$ velocity signal along z for each fixed y-location, the wall-normal BL evolution ($\overline{u}_b$) is estimated at a fixed x/c. The freestream velocity $\overline{u}_\infty$ is extracted at x/c=0.165 as the average value of $\overline{u}_b$ for $y > \delta_{99}$, and is used to normalize all velocity components. The disturbance velocity field is then computed as $\overline{u}_d = \overline{u}(x, y, z) - \overline{u}_b(x, y)$. The wall-normal evolution of the perturbations, i.e. the disturbance velocity profile $\langle u \rangle_z$, is obtained as the root mean square (rms) of the $\overline{u}_d$ velocity signal along z [6, 33]. Finally, the spanwise velocity signal at each xy-location is transformed in the spatial Fourier space ($\mathrm{FFT}_z(\overline{u})$), characterizing the development of the dominant CFI mode and its harmonics. The total perturbation amplitude and the individual FFT modes amplitudes are estimated at each x-location by respectively integrating the $\langle \overline{u} \rangle_z$ profile or the corresponding FFT shape function along y [6, 34]. The integral amplitude provides an estimation of the near-wake stationary instabilities growth along the chord.

Parameter	PTV Set-up
Acquired domain	xyz Volume
Acquired x/c range	0.15-0.176
Field of view [mm]	30×3.8×30
Vector pitch [mm]	0.25×0.04×0.25
Magnification factor	0.41
Focal length [mm]	400
Numerical aperture ($f_\#$)	11
Spatial resolution [px/mm]	67
Sampling rate (f_s) [Hz]	10
Frame separation (Δt) [μs]	8
Freestream displacement [px]	10
Number of samples	4000
Uncertainty [% local speed]	1.8

Table 1 Parameters of experimental PTV acquisitions

Parameter	HWA Set-up
Acquired domain	yz Plane
Acquired x/c range	0.152-0.17
Field of view [mm]	2.5×24
y vector pitch [mm]	0.03-0.5
y vector pitch [mm]	0.3
x plane pitch [mm]	2.5
Sampling rate (f_s) [kHz]	51.2
Measured interval (Δt) [s]	2
Uncertainty [% local speed]	0.13

Table 2 Parameters of experimental HWA acquisitions

3. Hot Wire Anemometry (HWA)

Hot wire anemometry (HWA) is employed to complement the steady near-element flow topology investigation, allowing for the local acquisition of temporally-resolved unsteady velocity fields. The HWA measurement system consists of a single-wire BL probe (Dantec Dynamics 55P15), operated using a TSI IFA-300 constant temperature bridge with automatic overheat ratio adjustment. The probe is mounted onto a three degree-of-freedom traversing system with positioning precision of 2.5μm. The system is calibrated every 24 hours and freestream conditions are continuously monitored to ensure proper BL measurements.

A series of wall-normal yz planes are measured at successive chord locations (x/c=0.152-0.17) using an ensemble of hot wire scans. Each plane consists of 32 measurement points in the wall-normal direction with y-spacing between points progressively refined as moving from the freestream towards the wall. After the acquisition of a single BL profile, extending from 15%U_∞ to the freestream, the probe is moved to its next spanwise location where the BL scan repeats. This process is carried out for the entire spanwise extent of a measurement plane, namely z/λ_1=3, maintaining a

Downloaded by TU DELFT on January 24, 2023 | http://arc.aiaa.org | DOI: 10.2514/6.2023-2306

spanwise spatial resolution of 0.3mm. Preliminary examination of the flow field performed by using the IR images (such as those reported in figure 2), allows for an overview of the developing near-element structures, and enables precise positioning of each measurement plane. Additionally, a coarser hot wire scan at x/c=0.2 is acquired to characterize downstream instability development.

Throughout the measurements, the hot wire probe is aligned with the Z-axis of the wind tunnel system, and as a result measures a projected velocity whose magnitude can be constructed as:

$$U(y,z) = \sqrt{(u \times cos(45°))^2 + (w \times sin(45°))^2 + (v)^2} \tag{1}$$

The instantaneous velocity field is sampled at 51.2kHz for 2s at each measurement point and is separated into a time-averaged $\overline{U}$ and fluctuating U' component. The resulting stationary and unsteady velocity fields are non-dimensionalized by the time-averaged freestream velocity $\overline{U}_\infty$ at the corresponding chordwise location. An averaging of the velocity profiles in the undisturbed regions located between elements, is used to estimate the locale laminar BL profile $\overline{U}_b$ (as shown in figure 1). This is then linearly extrapolated to determine the location of the wall, interpreted as the y-location where $\overline{U}_b = 0$.

The processing of the time-averaged $\overline{U}$ velocity signal, follows a procedure comparable to that described for the PTV velocity fields. As detailed in section § III.A, the stationary flow characteristics acquired by PTV and HWA are comparable. Therefore, the HWA acquisitions are exploited to build upon the steady PTV data and incur the unsteady disturbances topology, main characteristics and evolution. The temporal standard deviation of the HWA velocity fields $U'(y,z)$ is used to identify regions of high fluctuation intensity. Spectral analysis is carried out using Welch's periodogram [35] method to estimate the power spectral density (PSD) of the velocity signals, with frequency bins of 25Hz. The total fluctuation energy E'_{tot} and the modal fluctuation energy E'_f at a particular frequency f, are estimated by integrating the velocity PSD in the spatial domain and over the whole considered f range or within a 250Hz band centred around f respectively [22]. The extracted energy values are non-dimensionalized by $\overline{U}^2_\infty$ and provide an estimation of the unsteady disturbance energy evolution within the considered domain.

III. Steady Near-Element Flow Topology

A. Baseflow Topology and Transitional Behavior

The base flow characteristics are at first assessed by comparing the BL velocity profiles extracted from the 3D-PTV acquisitions with the numerical BL solution. As a representative example, figure 1(a) reports the $\overline{u}_d$ contours acquired through 3D-PTV in the yz plane at x/c=0.153. The flow features pertaining to the presented case are thoroughly discussed in §III.B, however, the velocity field is shown here to facilitate the understanding and visualization of the presented BL flow analysis. In particular, the contours of figure 1(a), indicate that at the considered location the portion of the BL developing "in between" two DREs is only marginally affected by the introduced velocity disturbances. Therefore, three in-between spanwise locations are chosen as representative for the BL development investigation. BL profiles as acquired by 3D-PTV and as numerically obtained from the BL solver are projected in the HWA reference frame following equation 1, and are normalized by the corresponding freestream velocity $\overline{U}_\infty$ (figure 1(b,c)). For representative reasons, the BL velocity profiles are shifted along the z-axis such that their velocity value at the wall corresponds to the location at which they are extracted. In the element vicinity, i.e. figure 1(b), the experimental and the numerical BL profile are in good agreement. This ensures that the boundary layer and its stability characteristics are comparable between the current work, previous investigations and numerical results. However, the more downstream location considered in figure 1(c), indicates that the velocity disturbances introduced by each DRE spread along the span and affect the whole BL development. In fact, the experimental $\overline{U}_b$ profile shape is deformed and shows the typical features of a perturbed, almost turbulent, BL.

To ensure the comparability of the 3D-PTV and HWA acquisitions, the assessment of the HWA-measured BL development is as well reported in figure 1(b, c). The similarities between the normalized $\overline{U}_b$ as extracted from 3D-PTV (- line) and HWA (∘), is indicative of the baseflow comparability among the two different measurement techniques. This allows for complementing the stationary instability analysis provided by the 3D-PTV acquisition, with the unsteady instabilities investigation provided by HWA.

The acquired IR images further characterize the perturbed BL flow topology (figure 2). The wide-angle lens (figure 2(a)) captures a global overview of the transition scenario, with a uniform region of lower wall-temperature (dark) extending from x/c≃0.17 to the end of the domain. This is indicative for the early onset of turbulence in the

Downloaded by TU DELFT on January 24, 2023 | http://arc.aiaa.org | DOI: 10.2514/6.2023-2306

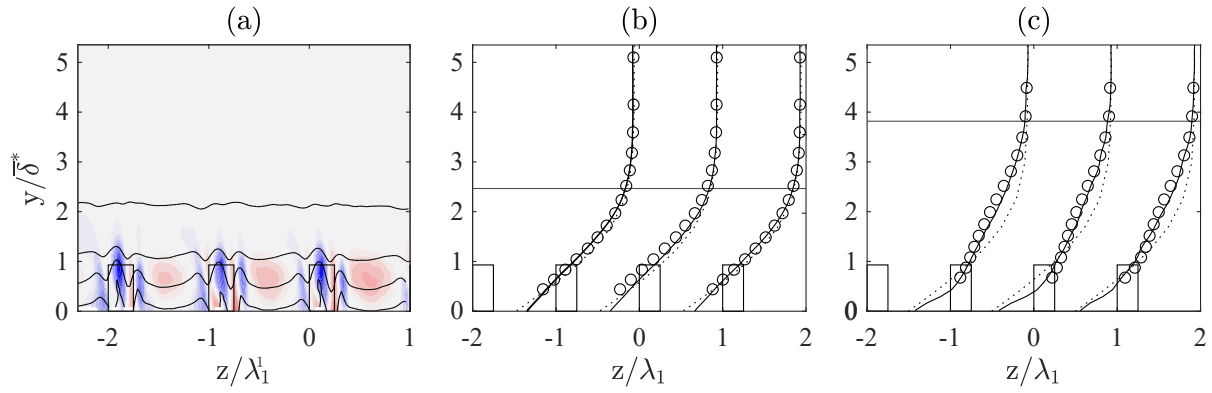

Fig. 1 (a) Contours of $\overline{u}_d$ extracted from 3D-PTV in the yz plane at x/c=0.153. Numerical unperturbed BL solution (··), 3D-PTV (–) and HWA (○) $\overline{U}_b$ velocity profiles extracted at (b) x/c=0.153 and (c) x/c=0.17. Rectangles represent the DRE location and shape, horizontal line is experimental δ_{99}.

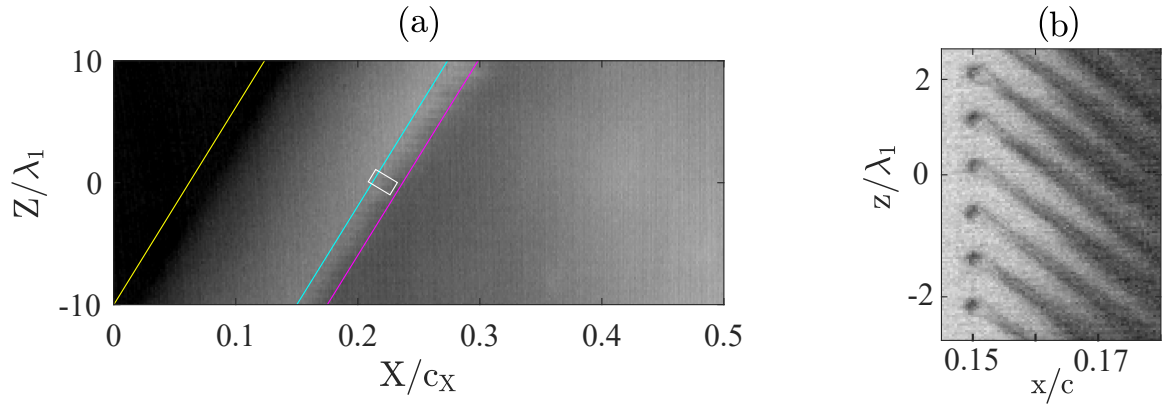

Fig. 2 IR thermography fields acquired using (a) wide-angle and (b) zoom lens configuration. Flow comes from the left; leading edge (yellow line), DRE location (blue line) and transition front (pink line). White square represents zoomed-in region of (b).

vicinity of the DRE array, as expected for a super-critical Re_k configuration. The close-up image of the DRE array (figure 2(b)) allows for an indicative description of the near-element flow topology. A pair of dark streaks can be identified on either side of each cylindrical element, corresponding well to the footprints of the strong HSV system legs pertinent to a super-critical forcing [12]. These streaks merge shortly downstream of the element, originating a turbulent wedge at x/c≃0.16 that progressively expands in the spanwise direction. The individual wedges eventually merge with neighbouring wedges further downstream (at x/c≃0.175), initiating the BL transition. The identified flow topology is further discussed hereafter with the help of the acquired local velocity fields.

B. Steady Near-Element Flow Topology

The acquired 3D-PTV velocity fields are considered hereafter to outline the stationary near-element flow topology, characterizing the onset and evolution of the stationary disturbances in the element vicinity. The stationary flow fields incurred by the considered DRE array, are described by the time-averaged disturbance velocity field ($\overline{u}_d$) in figures 3(a-c), while figures 3(d-f) show the standard deviation contours (u').

The disturbance velocity contours of figures 3(a) are acquired in the wall-parallel xz plane, and show that a low-speed wake develops immediately aft of each DRE. This low-speed region is initiated in correspondence of the recirculation region located aft of the element, and briefly extends further downstream in the element's wake. Additionally, two high-speed streaks form and initially develop along both sides of the low-speed wake. The $\overline{u}_d$ and u' contours acquired

Downloaded by TU DELFT on January 24, 2023 | http://arc.aiaa.org | DOI: 10.2514/6.2023-2306

Downloaded by TU DELFT on January 24, 2023 | http://arc.aiaa.org | DOI: 10.2514/6.2023-2306

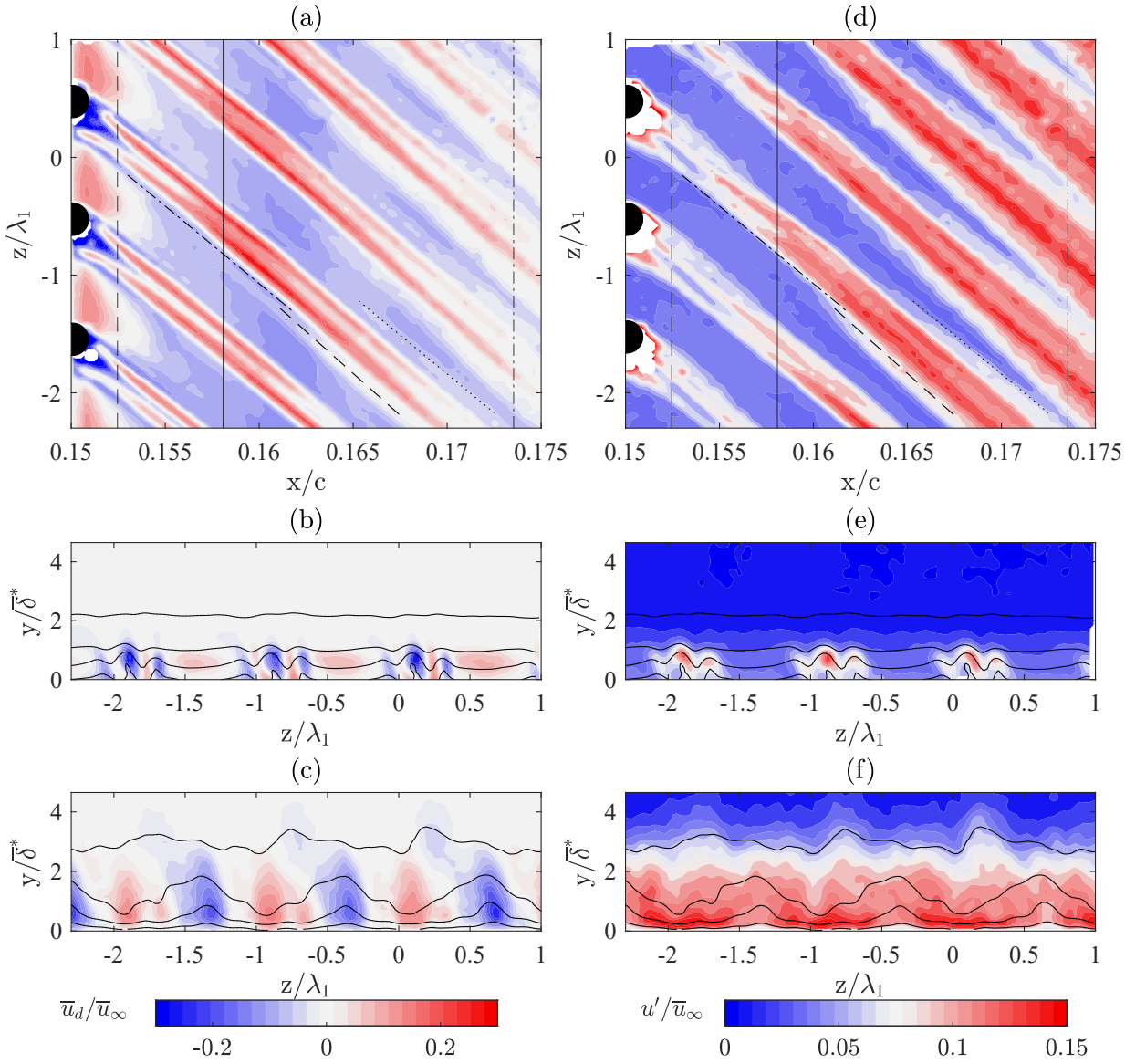

Fig. 3 Contours of (a-c) $\overline{u}_d$ and (d-f) u' extracted in (a, d) the xz plane at y=0.17$\overline{\delta}_{99}$; and extracted (b, e) in the yz plane at x_1/c=0.153 (vertical dashed line in (a)), and (c, f) at x_2/c=0.174 (vertical dash-dot line). Vertical full line at x/c=0.158.

in the wall-normal plane (figure 3(b, e)) confirm that, thanks to the highly localized velocity disturbances introduced by each DRE, in between elements the developing BL retains a laminar behaviour. However, shortly downstream of the element location (i.e x/c≃0.158, vertical black line in figure 3(a)) the two high-speed streaks merge and substitute the low-speed wake. This separates the near-wake region (x/c<0.158), dominated by the streaks evolution, from the far-wake region (x/c>0.158) of the flow field, characterized by the turbulent wedge onset. As growing further downstream, the high-speed wake appears to expand along the spanwise and wall-normal direction, as also visible in figure 3(c, f). This behaviour strongly resembles the flow topology and evolution observed for isolated DRE of super-critical amplitude both in 2D and 3D boundary layers [12, 15, 36, 37].

The standard deviation fields (figures 3(d-f)) indicate that in the near-wake (i.e. x/c<0.158) the regions of higher unsteadiness are mostly located in between the identified streak structures, where wall-normal and spanwise shears are the highest. More specifically, the near-wake is characterized by the development of a high-fluctuation locii in between the low-speed region and the high-speed streaks ([15, 36]). This correspondence suggests that the disturbances

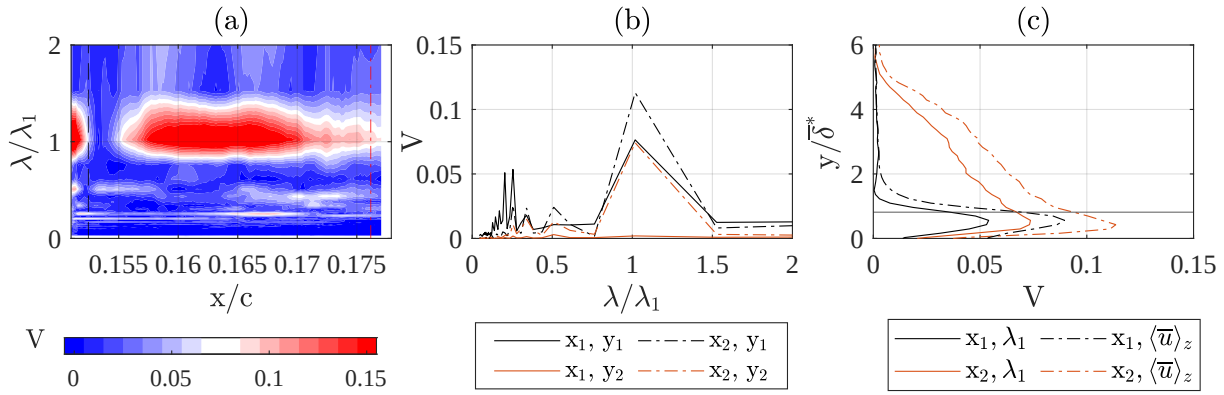

Fig. 4 FFT spectra (a) in the x-λ_z plane; (b) at fixed xy locations with x_1/c=0.153; x_2/c=0.174; $y_1/\overline{\delta}^*$=0.6; $y_2/\overline{\delta}^*$=1.8. (c) $\langle\overline{u}\rangle_z$ profiles and λ_1 FFT shape function at x_1 and x_2. V stands for FFT$_z(\overline{u})/\overline{u}_\infty$; element height (horizontal full line).

initiated in the near-wake strongly correlate to the wall-normal and spanwise shear layers developing in the recirculating flow region [13, 37]. The formation and initial growth of the high-speed wake, is accompanied by an increase of the corresponding fluctuations level. In fact, downstream of x/c=0.158, the higher fluctuations locii, corresponding to the outboard high-speed streak, rapidly spreads along the spanwise and wall-normal directions, occupying the whole high-speed wake region (figure 3(d,f)). This behavior is typically associated to the breakdown of the identified laminar streak structures and the onset of turbulence [15, 38]. Accordingly, each DRE appears to initiate a turbulent wedge at a finite distance from the element (i.e. x/c≃0.16, [15]), which downstream evolution locally corresponds to their high-speed, high-fluctuations wake. The u' spatial organization and evolution, shows that the initiated high-fluctuation region develops along a 6° inboard tilted trajectory. This is in agreement with previous investigations [12, 37], and can be related to the suppression of the flow structures counter-rotating with the baseflow crossflow velocity component. The resulting flow asymmetry is identifiable in the turbulent wedge opening, which is as well tilted towards the inboard direction.

Additionally, the reported $\overline{u}_d$ contours (figure 3(a)) show that the spanwise expansion of the high-speed region, is associated to a cascade of low- and high-speed streaks progressively developing on the high-speed wake's sides [39]. In particular, shortly downstream of the DRE location, in correspondence of the element's wake inboard side, a low-speed streak is initiated (dashed-dot line in figure 3(a)). This streak persists along the high-speed wake up to x/c≃0.16, where a high-speed streak forms on its inboard side. The latter rapidly grows, and merges with the high-speed wake shortly downstream. A comparable, albeit weaker, mechanism drives the high-fluctuations region opening towards the outboard direction (dotted line in figure 3(a)), further confirming the asymmetric flow field development. By comparing the identified stationary flow topology to the u' contours, the development of the high-speed streaks generally corresponds to a localized increase in the fluctuations level. This indicates that the identified streak cascade drives the spanwise expansion of the high-fluctuations region (figure 3(d)). Nonetheless, in the current configuration the role of the wedge-opening mechanism described beforehand is limited by the flow periodicity: due to the finite DRE inter-spacing the wedges initiated by each element, already merge with neighbouring ones towards the end of the acquired domain (i.e. x/c≃0.174), leading to the formation of a spanwise transition front (figure 3(f)).

The results reported so far clearly characterize the near-wake stationary flow topology, confirming the IR visualization of figure 2(b). However to further investigate the occurring transitional process and the nature of the dominant flow instabilities, the spectral composition of the BL is analysed hereafter.

C. Spectral Analysis and Steady Transient Instabilities

The spectral composition of the near-element flow region can be investigated by applying a spanwise spatial FFT to the time-averaged velocity signal for each of the three acquired componentli s (§II.B.2). This allows for the identification of the dominant stationary disturbance modes as well as for the characterization of the individual FFT modes downstream evolution.

Figure 4(a) reports the spatial FFT spectra in the x-λ_z plane at y/$\overline{\delta}^*$=0.6. High spectral energy pertains to the forced

Downloaded by TU DELFT on January 24, 2023 | http://arc.aiaa.org | DOI: 10.2514/6.2023-2306

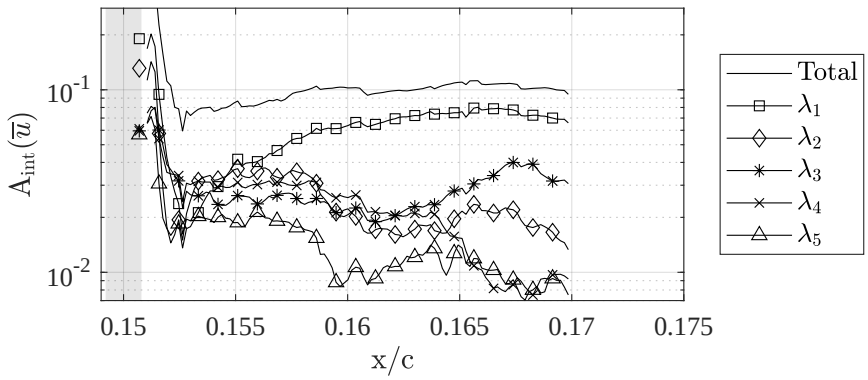

Fig. 5 $A_{int}(\overline{u})$ for the total disturbance field and for the $\lambda_1 - \lambda_5$ FFT harmonics. Shaded region represents the element location.

Downloaded by TU DELFT on January 24, 2023 | http://arc.aiaa.org | DOI: 10.2514/6.2023-2306

mode λ_1 both in the near-wake and far-wake flow region. Nonetheless, a wide set of higher harmonics is also developing throughout the whole considered domain. In the far-wake flow evolution (i.e. x/c>0.158), the high harmonics content can be attributed to the laminar structures breakdown and the progressive onset of turbulence in correspondence of the element high-speed wake (dashed-dot spectra in figure 4(b)). However, the near-wake flow region is characterized by the presence of an even wider range of harmonic modes developing with comparable or higher spectral energy than the one pertaining to λ_1. This is clearly shown by the spatial spectra extracted at x_1/c=0.153 and x_2/c=0.174 reported as a black lines in figure 4(b). The presence of these harmonic modes can be related to the combination of the highly localized nature of the element's wake, acting as a pseudo-pulse, and the presence of two geometrical constraints: the finite diameter of the DRE and their inter-spacing. As such, it is important to note that the identified spectral FFT components do not necessarily correspond to the natural instability modes characterizing the near-wake flow. Nonetheless, they correctly represent the near-wake flow features in the modal FFT space.

Figure 4(b) also reports the FFT spectra extracted at a higher wall-distance ($y/\overline{\delta}^*$=1.8, red lines). No relevant modal content pertains to this flow region in the near-wake, indicating that the disturbances evolution is limited to the BL region closer to the wall. This agrees well with the $\overline{u}_d$ and u' contours of figure 3(b, e), and is further confirmed by the λ_1 mode shape function reported in figure 4(c). In fact, both in the near-wake and in the far-wake region the amplitude peak is reached at a wall-normal distance comparable with the element height. This y-location corresponds to the maximum fluctuations locii typically identified in the wake of isolated DREs [15, 37, 39]. Such correspondence confirms that the disturbances introduced in the element's wake relate to the enhanced shears and unsteadiness pertaining to the recirculation region developing aft of the element, rather than being related to modal instability mechanisms (as further discussed in §IV). Comparable wall-normal evolution is shown by the disturbance profile extracted from the full 3D-PTV field (i.e. $\langle\overline{u}\rangle_z$). However, despite the similar shape, at both considered chord locations the $\langle\overline{u}\rangle_z$ profile achieves higher amplitude values than the λ_1 shape function. This is in agreement with the significant harmonic content identified in the flow field, and can be the source of non-linear interactions in the downstream flow development.

As a last step for the characterization of the stationary near-wake disturbances, the estimation of the total disturbance amplitude ($A_{int}(\overline{u})$) as well as of the individual FFT modes amplitude ($A_{int,\lambda_i}(\overline{u})$) is reported in figure 5. Immediately aft of the element, both the A_{int} and the considered A_{int,λ_i} decay due to the presence of the strong low-speed region characterizing the element's wake. Further downstream (i.e. x/c≃0.152), the total disturbance amplitude starts recovering, following a mild growth trend. This is slowed down and interrupted towards the end of the considered domain due to the laminar structures breakdown. The amplitude trend of the dominant λ_1 mode follows, instead, a different evolution. Specifically, the amplitude recovery occurs in a slower fashion and at more downstream chord locations (i.e. x/c≥0.158). Hence, in the near wake region, the λ_1 mode retains lower amplitude values despite the total amplitude growth.

Nonetheless, the higher harmonic modes reported in figure 5, all show a mild amplitude increase in the near-wake region (between x/c≃0.152-0.158), while they all decay further downstream in agreement with the modal stability solution prediction (LST, [25]). The behavior of the total amplitude combined with the dominant and higher harmonic modes evolution, is indicative of the presence of stationary transient disturbances in the near-wake flow evolution [10, 14, 40, 41]. Specifically, transient growth phenomena have been observed to condition the near-wake evolution of DRE elements both in critical and super-critical 2D boundary layers [9, 40, 41].

Typically, in super-critical forcing scenarios the presence of transient growth is related to the rapid growth of the near-wake disturbances, which actively contribute to initiate the laminar breakdown and the onset of turbulent flow [9]. However, in the super critical roughness configuration considered in the current work, the stationary transient disturbances are not sufficiently strong to induce an explosive $A_{int}(\overline{u})$ growth that could motivate the observed laminar structures breakdown. This can be related to the fact that the stationary disturbances characterized beforehand, only give a partial insight on the transitional process and on the nature of the instabilities responsible for its occurrence. Specifically, the amplitude trends reported in figure 5 show that the rapid recovery of the dominant mode, occurs in proximity of the high-speed and streaks cascade formation (i.e. at x/c≃0.158). This process drives the increase of the overall fluctuations level, which is indicative of the growth of the unsteady wake disturbances [16, 37]. The time-averaged nature of the 3D-PTV measurements presented up to this point, does not allow for more detailed investigation of the role of the unsteady disturbances in the transitional process. Therefore, given its relevance for the near-wake flow development, this aspect is further investigated in the following section through HWA measurements.

IV. Unsteady Near-Element Flow Topology

As shown in §III.A, the steady boundary layer features measured by 3D-PTV and HWA are highly comparable. Hence, high-resolution HWA measurements are hereafter employed to complete the characterization of the near-element instabilities by analysing the unsteady disturbances fields.

The standard deviation of the HWA velocity signal U' is initially considered to identify the high-fluctuation regions forming in the DRE vicinity. The U' contours are presented for various chord locations in figure 6, with the z coordinate spanwise shifted as considering downstream planes to follow the evolution of the flow structures. Overall, the unsteady flow topology agrees well with the preliminary observations offered by the 3D-PTV acquisitions (figure 3(d-f)). Specifically, immediately aft of the element (i.e. x/c=0.152 figure 6(a)), an area of strong unsteadiness develops on top of each DRE. This locii of enhanced fluctuations, can be correlated with the presence of cylinder eddy shedding in the element wake, as previously observed for isolated DREs [15, 16, 37]. As evolving downstream (i.e. x/c=0.154-0.158), this region progressively grows in amplitude as well as in geometrical size, diffusing within the BL flow region. Furthermore, downstream of x/c=0.154, two additional regions of high unsteadiness are identified on either side of each DRE. These are located in correspondence of the high-shear regions forming along the element's flanks, and initially grow individually (i.e. x/c=0.156-0.158). Nonetheless, the three identified high-fluctuation regions rapidly spread in the spanwise and wall normal direction, occupying the whole DRE wake at x/c=0.16. It is worth noting that at this chord location the stationary high-speed streaks have already merged, substituting the DRE low-speed wake. This provides the conditions for the rapid spatial and amplitude growth of the unsteady instabilities, which initiate the breakdown of the laminar structures. This results in the onset of a turbulent wedge in correspondence of the stationary high-speed wake region, already visible at x/c=0.162 (figure 6(f)) where high-unsteadiness pertains to the whole DRE wake. The unsteady flow region, indicates that the turbulent wedge rapidly expands towards the neighbouring elements, driven by the stationary high-/low-speed cascade observed in figure 3(a, d). At x/c = 0.168 the individual turbulent wedges initiated by each DRE begin to merge. Shortly downstream, the whole BL flow region has transitioned to a turbulent state.

The high-fluctuation locii on top of each DRE can be further characterized analysing its frequency (i.e. temporal spectra) content. The temporal spectra of the velocity signal are computed as PSD using the Welch [35] periodogram procedure as discussed in § II.B.3. Representative PSD spectra are extracted at the locations of maximum unsteadiness identified on top of the central DRE, marked by a black cross (+) at each chordwise location in figure 6. One sample PSD spectra extracted in the freestream flow region at x/c=0.152 is as well reported (grey line), showing a significantly lower fluctuation energy level if compared to the DRE wake. Nonetheless, the freestream spectral distribution features a relevant energy peak within the f≃10-11kHz band. Such frequency range is excited in all of the reported spectra, and can be attributed to the electronic characteristics of the bridge rather than being representative for physical flow phenomena [25, 42].

Overall, the near-wake region (i.e x/c=0.152-0.158) shows a strongly tonal behavior, with a dominant frequency peak within the f_1 ≃5.5-6kHz band accompanied by the presence of secondary peaks at its harmonics (shaded regions in figure 7). At downstream x/c locations, the dominant peak and its harmonics diffuse towards a more broadband spectra, indicative of the onset of turbulence. The local Strouhal number defined as $St_{\overline{\delta}^*} = \frac{f\overline{\delta}^*}{|\mathbf{u}(k)|}$, is used to compare the spectral content of the flow to results established in literature. The dominant tone in the element vicinity is seen to lie within $St_{\overline{\delta}^*}$≃0.17-0.18 which is close to the shedding range of a circular cylinder ($St_{\overline{\delta}^*}$≃0.18-0.25) as reported by Klebanoff et al. [15] and Kuester and White [43]. This correspondence indicates that the mechanism dominating the

Downloaded by TU DELFT on January 24, 2023 | http://arc.aiaa.org | DOI: 10.2514/6.2023-2306

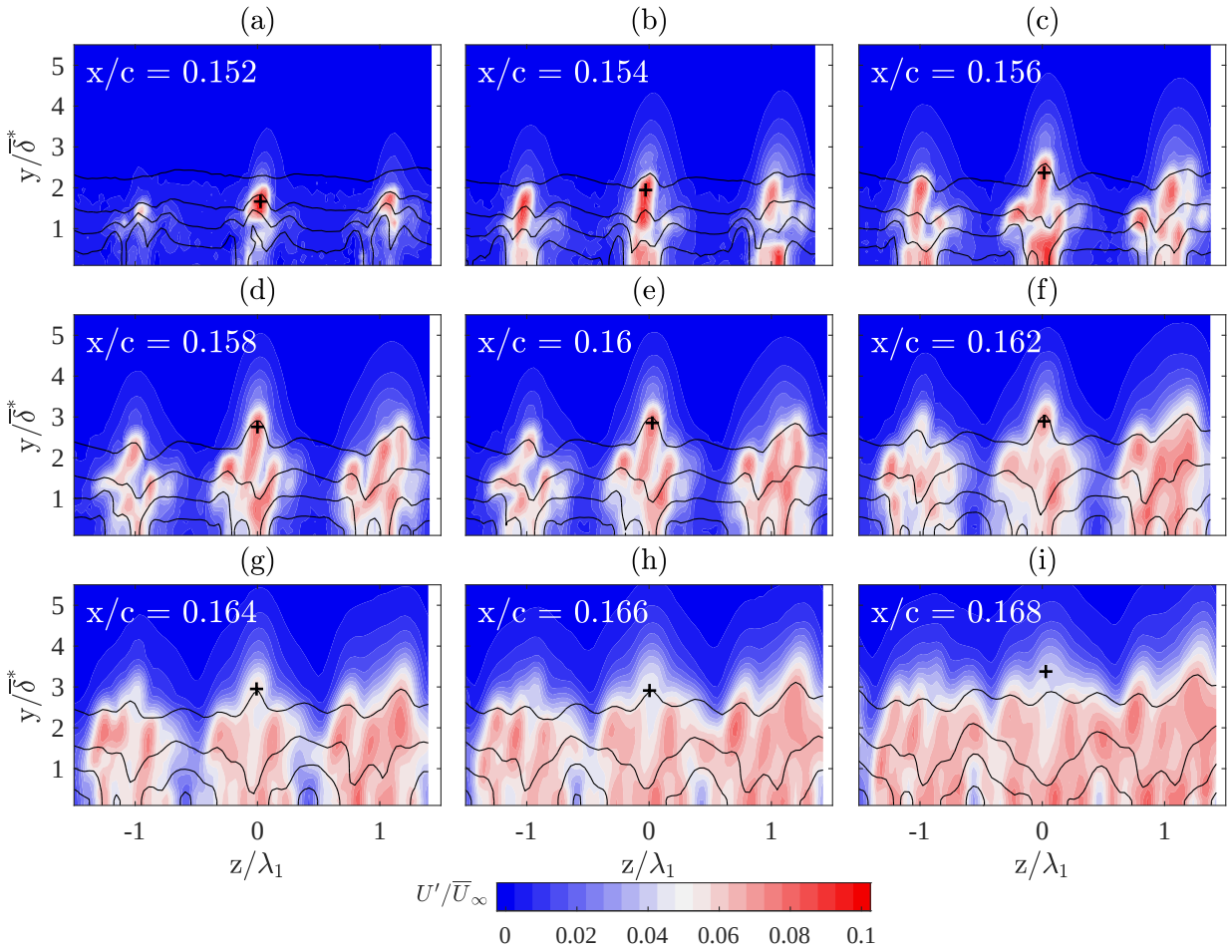

Fig. 6 Contours of U' at various x/c locations; steady velocity isolines $\overline{U}/\overline{U}_\infty$ every 20%$\overline{U}_\infty$ (full lines). Maximum fluctuation location on top of the element (+).

instability onset and development in the super-critical near-wake, can be associated to element shedding. The initiated near-wake instabilities are rapidly amplified in the element vicinity, likely reaching non-linear amplitudes and becoming the driver for the laminar breakdown and the turbulence onset. Comparable observations are reported by Kurz and Kloker [12], Bucci et al. [44] or Zoppini et al. [37], identifying an amplifier behavior of the element near-wake region for configurations characterized by low freestream disturbances (i.e. low T_u levels). Additionally, the spectra reported in figure 7 show that the dominant frequency peak is relatively broad in the element vicinity. This indicates that a small range of frequencies is excited in the near-wake, initiating a range of instability modes that possibly grow due to non-modal interactions and transient phenomena [9, 44, 45]. The Strouhal number loses its significance further downstream, as the broadband turbulent spectrum becomes more prevalent.

To further quantify the evolution of unsteady instabilities in the DRE vicinity, the spectral power of the acquired point-wise velocity signal, provided by the performed Welch's periodogram analysis, is considered. By spatially integrating in the zy plane the PSD values corresponding to each frequency, the associated integral energy (named E' and non-dimensionalized by $\overline{U}_\infty^2$) in the frequency space is obtained. The $E'/\overline{U}_\infty^2$ contours are reported in figure 8(a), using a logarithmic scale for visualization purposes. In the near-wake region (i.e. x/c=0.152-0.158), high energy peaks are visible in correspondence of f_1 ≃5.5-6kHz and its f_2 to f_4 harmonics, confirming the strongly tonal behavior identified from the spectral analysis (figure 7). The chordwise growth of the unsteady instabilities is initially accompanied by the energy growth of the sole dominant frequencies. Nonetheless, a global energy increase, spread over the whole considered frequency bandwidth, can be observed downstream of x/c=0.16. This agrees well with the observed spreading of the high-fluctuations region and the onset of turbulent flow.

Downloaded by TU DELFT on January 24, 2023 | http://arc.aiaa.org | DOI: 10.2514/6.2023-2306

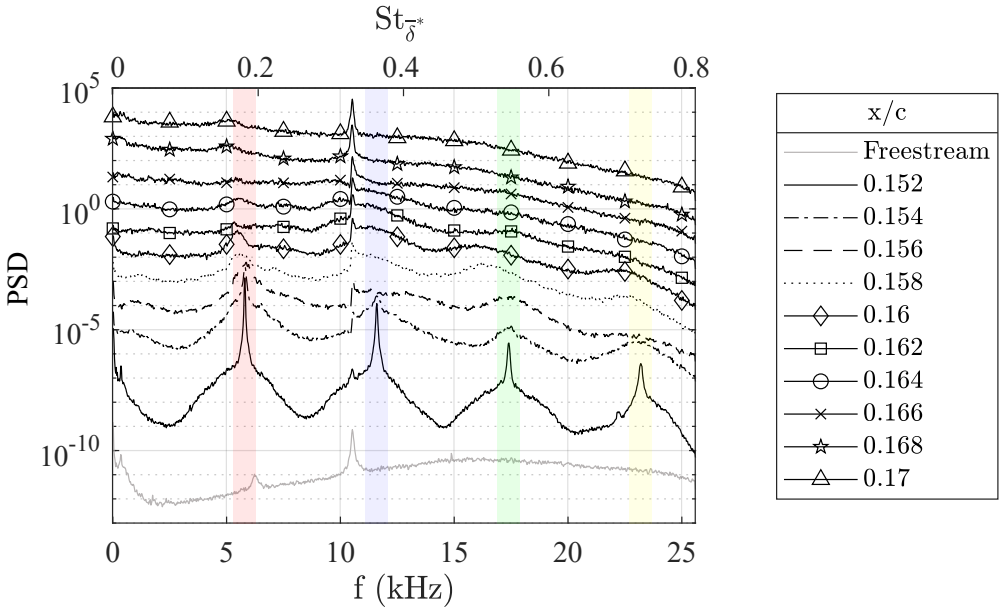

Fig. 7 Frequency spectra extracted at different x/c locations in correspondence of the maximum fluctuation location on top of the element (+ in figure 6). For visualization purposes, the spectra at each chord location is offset by a decade. Freestream flow frequency spectra extracted at x/c=0.152 (gray line, no offset); spectral peak and harmonics (shaded regions).

To isolate the behavior of the dominant modes and compare it to the overall unsteady instability evolution, the total unsteady energy E'_{tot} and the modal unsteady energy E'_{f} at the fundamental frequency band f_1 and its harmonics are extracted. E'_{tot} is computed by integrating the E' over the whole frequency band considered, while the modal energy only integrates E' within the corresponding frequency band. The resulting trends are presented in figure 8(b). The super-critical DRE forcing introduces a strong level of unsteadiness into the low-speed wake, with E'_{tot} mildly growing within the acquired domain and reaching an almost constant level towards the domain end. This resembles the results presented by Ergin and White [22] for a super-critical forcing case in a 2D boundary layer, where the unsteady fluctuation energy is observed to exponentially grow in the element vicinity and saturate with the onset of turbulence. The initial exponential growth phase is not identifiable in the reported energy curve. However, the growth of the unsteady instabilities is strongly linked to the wall-normal and spanwise velocity shears, which in the element vicinity are sufficiently strong to cause a rapid (likely exponential) growth of the unsteady instabilities. Hence, the unsteady energy measured at the first acquired (and presented) location x/c=0.152 is already close to the saturation level.

Similar behavior can be observed for the energy evolution of the fundamental frequency band E'_{f_1}, which contains most of the disturbance energy in the element near-wake. Comparably to E'_{tot}, the rapid initial growth phase is not identified in the presented curves. However, E'_{f_1} continuously grows up to x/c=0.155, before mildly decaying to an almost constant value at x/c≃0.16. This transitory growth is also identifiable in the E' contours of figure 8(a), and can significantly contribute to the rapid enhancement of the near-wake instabilities. The mild decay and asymptotic behavior of E'_{f_1} are indicative of the diffusion of the shedding peak towards the broadband turbulent spectra, geometrically correlating to the high-fluctuation locii on the element top and its diffusion within the element wake. This process is initiated at a chord location comparable to the high-speed wake formation and the turbulent wedge onset. The unsteady energy pertaining to the higher harmonic bands follows comparable trends, with a rapid growth in the element vicinity and saturation around x/c=0.16, confirming the onset of turbulence at this chord location.

The identified behavior, indicates that the unsteady instabilities introduced in the near-wake by the element shedding, are rapidly amplified to non-linear and saturated energy levels. Furthermore, the steady near-element flow, features high steady energy levels and an inherent instability that in a critical state (accompanied by lower unsteadiness) would evolve into modal CFI. Hence, in the investigated scenario the unsteady fluctuations rapidly reach transitional amplitudes that can condition the near-wake evolution, preventing the steady state relaxation to a condition stable to high-frequency disturbances and initiating the transitional process [22].

Downloaded by TU DELFT on January 24, 2023 | http://arc.aiaa.org | DOI: 10.2514/6.2023-2306

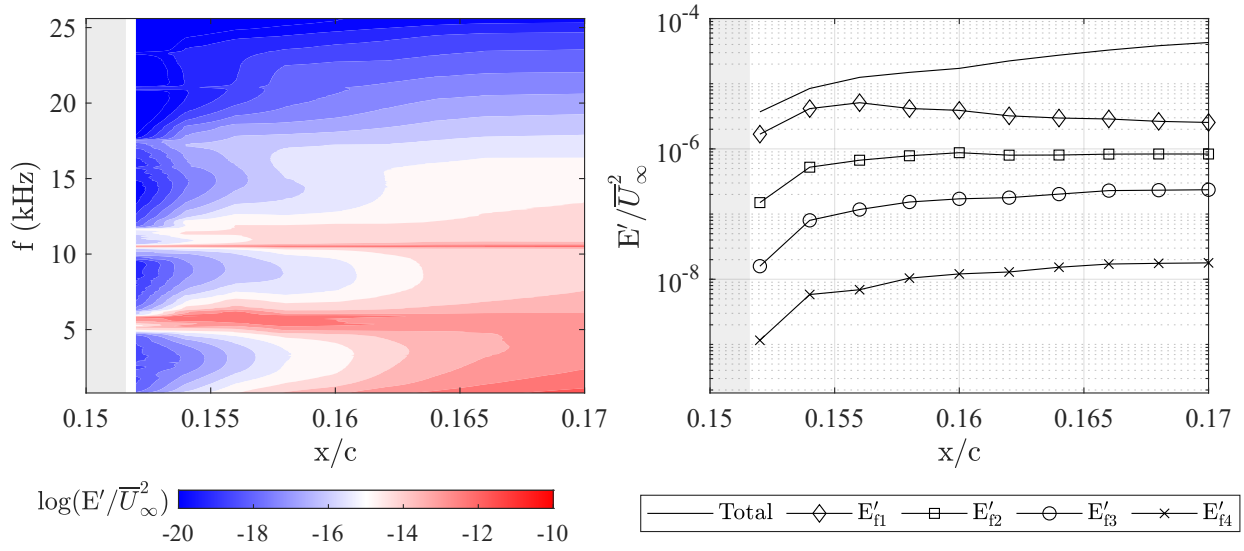

Fig. 8 (a) Contours of E'/$\overline{U}_\infty^2$ in the x-f domain. (b) Chordwise evolution of E'$_{tot}$ and E'$_f$ for the f_1-f_4 frequency bands. Element location (shaded region).

V. Conclusions

The presented investigation characterizes the stationary and unsteady flow evolution in the vicinity of a super-critical DRE array located at x/c=0.15 in a swept wing BL.

Experimental 3D-PTV acquisitions, indicate that the stationary near-wake is dominated by the formation of a low-speed wake immediately aft of the DRE, accompanied by two high-speed streaks developing on its sides. Shortly downstream (i.e. x/c≃0.158), the high-speed streaks merge and continue growing, substituting the low-speed wake. This results into enhanced unsteadiness originating a high-fluctuation region developing in correspondence of the high-speed wake and initiating a turbulent wedge. The formation of a high- and low-speed streaks cascade on the high-speed wake sides, is responsible for the progressive spanwise opening of the wedge region [39]. Due to the geometrical constraints introduced by the finite DRE spacing, the wedges initiated by individual elements merge along the span at x/c≃0.168.

A spanwise spatial FFT analysis identifies the presence of the dominant mode λ_1 and a set of harmonics developing both in the near-wake and far-wake region. Spectral energy analysis, suggests that transient mechanisms dominate the stationary near-wake evolution, affecting both the primary stationary mode and its harmonics. However, in this flow scenario the transient growth process occurs in conjunction with enhanced shears and excessive amplitude of the velocity disturbances developing in the near-wake region. Thus, the transient growth phenomena are not sufficiently strong to induce an explosive A_{int} growth that could motivate the observed laminar structures breakdown.

Therefore, the unsteady flow topology is detailed using the HWA measurements. High-fluctuations regions are identified on top and on the flanks of each DRE, mostly developing in correspondence of high-shear locii. These high-fluctuations regions grow further downstream, while expanding in the spanwise and wall-normal direction. At about x/c=0.160, in correspondence of the high-speed streaks merging, the three identified high-fluctuations regions merge as well, enhancing the overall wake unsteadiness and initiating the turbulent wedge development.

The spectral analysis of the time-dependent velocity signal, shows a tonal behavior dominates the near-wake flow development (upstream of the onset of turbulence). The $St_{\overline{\delta}^*}$ number computed based on the dominant frequency provides values that lay within the shedding range identified in literature [15]. Additionally, the frequency band corresponding to the shedding, contains most of the unsteady energy in the element vicinity. This indicates that the dominant near-wake instabilities are initiated by the shedding process occurring on the element top side. Specifically, both the total unsteady energy (E'$_{tot}$) and E'$_{f_1}$ undergoes a rapid exponential growth in the element vicinity, of which only the tail is visible in the reported domain. The two considered energy components saturate towards the end of the domain, nonetheless, E'$_{f_1}$ shows a mild transitory growth and decay which can contribute to the rapid amplification of the unsteady instabilities to non-linear regimes. The harmonic components follow a growth and saturation trend comparable to E'$_{tot}$. Overall, the saturation region of both the total and modal unsteady energy components, correlates

Downloaded by TU DELFT on January 24, 2023 | http://arc.aiaa.org | DOI: 10.2514/6.2023-2306

well with chord locations featuring a broadband spectra and unsteady fluctuations spread within the element wake. These effects are all indicative of the onset of turbulence, initiated as a turbulent wedge in the vicinity of x/c≃0.16 and developing within the element wake region. The wedge downstream growth, diffuses enhanced unsteadiness towards the whole BL region and throughout the considered spectral frequencies, causing transition shortly downstream of the element location. Hence, in the investigated scenario, the rapid growth of unsteady amplitudes and the inherent instability of the stationary wake, prevent the steady flow relaxation and the onset of modal instabilities. On the contrary, as discussed by Ergin and White [22], the unsteady instabilities are rapidly amplified to non-linear and saturated levels, driving the BL transitional process.

The authors are grateful to the European Research Council for financially supporting this research through the GLOWING Starting Grant (803082).

References

[1] Bippes, H., "Basic experiments on transition in three-dimensional boundary layers dominated by crossflow instability," *Progress in Aerospace Sciences*, , No. 35, 1999, pp. 363–412.

[2] Saric, W., Reed, H., and White, E., "Stability and transition of three dimensional boundary layers," *Annual Review of Fluid Mechanics*, Vol. 35, No. 1, 2003, pp. 413–440. https://doi.org/10.1146/annurev.fluid.35.101101.161045.

[3] Serpieri, J., and Kotsonis, M., "Three-dimensional organisation of primary and secondary crossflow instability," *Journal of Fluid Mechanics*, Vol. 799, 2016, pp. 200–245. https://doi.org/10.1017/jfm.2016.379.

[4] Wassermann, P., and Kloker, M., "Mechanisms and passive control of crossflow-vortex-induced transition in a three-dimensional boundary layer," *Journal of Fluid Mechanics*, Vol. 456, 2002, pp. 49–84.

[5] Morkovin, M., "On the many faces of transition," *Viscous drag reduction*, Springer, 1969, pp. 1–31.

[6] Reibert, M., Saric, W., Carrillo, J., and Chapman, K., "Experiments in nonlinear saturation of stationary crossflow vortices in a swept-wing boundary layer," *34th Aerospace Sciences Meeting and Exhibit*, American Institute of Aeronautics and Astronautics, 1996. https://doi.org/10.2514/6.1996-184.

[7] Saric, W., Carrillo, R., and Reibert, M., "Leading-edge roughness as a transition control mechanism," , 1998. https://doi.org/10.2514/6.1998-781.

[8] Gregory, N., and Walker, W., *The effect on transition of isolated surface excrescences in the boundary layer*, HM Stationery Office, 1956.

[9] White, E. B., Rice, J. M., and Gökhan Ergin, F., "Receptivity of stationary transient disturbances to surface roughness," *Physics of Fluids*, Vol. 17, No. 6, 2005, p. 064109.

[10] Zoppini, G., Westerbeek, S., Ragni, D., and Kotsonis, M., "Receptivity of crossflow instability to discrete roughness amplitude and location," *Journal of Fluid Mechanics*, Vol. 939, 2022. https://doi.org/10.1017/jfm.2022.220.

[11] Zoppini, G., Michelis, T., Ragni, D., and Kotsonis, M., "The near-wake of discrete roughness elements on swept wings: tomographic ptv measurements," *12th International Symposium on Turbulence and Shear Flow Phenomena (TSFP12)*, 2022.

[12] Kurz, H., and Kloker, M., "Mechanisms of flow tripping by discrete roughness elements in a swept-wing boundary layer," *Journal of Fluid Mechanics*, Vol. 796, 2016, pp. 158–194. https://doi.org/10.1017/jfm.2016.240.

[13] Brynjell-Rahkola, M., Schlatter, P., Hanifi, A., and Henningson, D., "Global Stability Analysis of a Roughness Wake in a Falkner-Skan-Cooke Boundary Layer," *Procedia IUTAM*, Vol. 14, 2015, pp. 192–200. https://doi.org/10.1016/j.piutam.2015.03.040.

[14] Landahl, M., "A note on an algebraic instability of inviscid parallel shear flows," *Journal of Fluid Mechanics*, Vol. 98, No. 2, 1980, pp. 243–251.

[15] Klebanoff, P. S., Cleveland, W. G., and Tidstrom, K. D., "On the evolution of a turbulent boundary layer induced by a three-dimensional roughness element," *Journal of Fluid Mechanics*, Vol. 237, 1992, pp. 101–187. https://doi.org/10.1017/s0022112092003379.

[16] Acarlar, M., and Smith, C., "A study of hairpin vortices in a laminar boundary layer. Part 1. Hairpin vortices generated by a hemisphere protuberance," *Journal of Fluid Mechanics*, Vol. 175, 1987, pp. 1–41.

Downloaded by TU DELFT on January 24, 2023 | http://arc.aiaa.org | DOI: 10.2514/6.2023-2306

[17] Kuester, M. S., and White, E. B., "Roughness receptivity and shielding in a flat plate boundary layer," *Journal of Fluid Mechanics*, Vol. 777, 2015, pp. 430–460. https://doi.org/10.1017/jfm.2015.267.

[18] Fischer, P., and Choudhari, M., "Numerical Simulation of Roughness-Induced Transient Growth in a Laminar Boundary Layer," *34th AIAA Fluid Dynamics Conference and Exhibit*, American Institute of Aeronautics and Astronautics, 2004. https://doi.org/10.2514/6.2004-2539.

[19] Cherubini, S., Tullio, M. D. D., Palma, P. D., and Pascazio, G., "Transient growth in the flow past a three-dimensional smooth roughness element," *Journal of Fluid Mechanics*, Vol. 724, 2013, pp. 642–670. https://doi.org/10.1017/jfm.2013.177.

[20] Schmid, P., and Henningson, D., *Applied Mathematical Sciences*, Springer-Verlag, New York, 2001.

[21] Ergin, G., Choudhari, M., Fischer, P., and Tumin, A., "Transient growth: Experiments, DNS and theory," 2005.

[22] Ergin, F., and White, E., "Unsteady and Transitional Flows Behind Roughness Elements," *AIAA Journal*, Vol. 44, No. 11, 2006, pp. 2504–2514. https://doi.org/10.2514/1.17459.

[23] Serpieri, J., and Kotsonis, M., "Design of a swept wing wind tunnel model for study of cross-flow instability," *33rd AIAA Applied Aerodynamics Conference*, American Institute of Aeronautics and Astronautics, 2015. https://doi.org/10.2514/6.2015-2576.

[24] Mack, L., "Boundary-layer linear stability theory," Tech. rep., California Inst of Tech Pasadena Jet Propulsion Lab, 1984.

[25] Serpieri, J., "Cross-Flow Instability," Ph.D. thesis, Technische Universiteit Delft, 2018. https://doi.org/10.4233/UUID:3DAC1E78-FCC3-437F-9579-048B74439F55.

[26] Malik, M., Li, F., Choudari, M., and Chang, C., "Secondary instability of crossflow vortices and swept-wing boundary-layer transition," *Journal of Fluid Mechanics*, Vol. 399, 1999, pp. 85–115. https://doi.org/10.1017/s0022112099006291.

[27] Reynolds, O., "On the extent and action of the heating surface of steam boilers," *Papers on Mechanical and Physical subjects*, 1901, p. 81.

[28] Rius Vidales, A., "Influence of a forward-facing step on crossflow instability and transition: An experimental study in a swept wing boundary-layer," Ph.D. thesis, 2022. https://doi.org/10.4233/UUID:6FD8A152-AB7A-4ECD-A817-61945D431BEF.

[29] Malik, N. A., and Dracos, T., "Lagrangian PTV in 3D flows," *Applied Scientific Research*, Vol. 51, No. 1, 1993, pp. 161–166.

[30] Wieneke, B., "Iterative reconstruction of volumetric particle distribution," *Measurement Science and Technology*, Vol. 24, No. 2, 2012, p. 024008. https://doi.org/10.1088/0957-0233/24/2/024008.

[31] Schanz, D., Gesemann, S., and Schröder, A., "Shake-The-Box: Lagrangian particle tracking at high particle image densities," *Experiments in Fluids*, Vol. 57, No. 5, 2016. https://doi.org/10.1007/s00348-016-2157-1.

[32] Wieneke, B., "Volume self-calibration for 3D particle image velocimetry," *Experiments in Fluids*, Vol. 45, No. 4, 2008, pp. 549–556. https://doi.org/10.1007/s00348-008-0521-5.

[33] Tempelmann, D., Schrader, L., Hanifi, A., Brandt, L., and Henningson, D., "Swept wing boundary-layer receptivity to localized surface roughness," *Journal of Fluid Mechanics*, Vol. 711, 2012, pp. 516–544. https://doi.org/10.1017/jfm.2012.405.

[34] Downs, R., and White, E., "Free-stream turbulence and the development of cross-flow disturbances," *Journal of Fluid Mechanics*, Vol. 735, 2013, pp. 347–380. https://doi.org/10.1017/jfm.2013.484.

[35] Welch, P., "The use of fast Fourier transform for the estimation of power spectra: A method based on time averaging over short, modified periodograms," *IEEE Transactions on Audio and Electroacoustics*, Vol. 15, No. 2, 1967, pp. 70–73. https://doi.org/10.1109/tau.1967.1161901.

[36] Loiseau, J., Robinet, J., Cherubini, S., and Leriche, E., "Investigation of the roughness-induced transition: global stability analyses and direct numerical simulations," *Journal of Fluid Mechanics*, Vol. 760, 2014, pp. 175–211. https://doi.org/10.1017/jfm.2014.589.

[37] Zoppini, G., Ragni, D., and Kotsonis, M., "Transition due to isolated roughness in a swept wing boundary layer," *Physics of Fluids*, Vol. 34, No. 8, 2022, p. 084113. https://doi.org/10.1063/5.0101187.

[38] Kendall, J., "Laminar boundary layer velocity distortion by surface roughness: Effect upon stability," *AIAA paper*, Vol. 195, 1981, p. 1981.

Downloaded by TU DELFT on January 24, 2023 | http://arc.aiaa.org | DOI: 10.2514/6.2023-2306

[39] Berger, A. R., and White, E. B., "Experimental Study of the Role of High- and Low-speed Streaks in Turbulent Wedge Spreading," American Institute of Aeronautics and Astronautics, 2020. https://doi.org/10.2514/6.2020-0832.

[40] Corbett, P., and Bottaro, A., "Optimal linear growth in swept boundary layers," *Journal of Fluid Mechanics*, Vol. 435, 2001, p. 1.

[41] Breuer, K. S., and Kuraishi, T., "Transient growth in two- and three-dimensional boundary layers," *Physics of Fluids*, Vol. 6, No. 6, 1994, pp. 1983–1993. https://doi.org/10.1063/1.868205.

[42] Saddoughi, S. G., and Veeravalli, S. V., "Hot-wire anemometry behaviour at very high frequencies," *Measurement Science and Technology*, Vol. 7, No. 10, 1996, pp. 1297–1300. https://doi.org/10.1088/0957-0233/7/10/002.

[43] Kuester, M., and White, E., "Structure of turbulent wedges created by isolated surface roughness," *Experiment in Fluids*, Vol. 57, 2016. https://doi.org/10.1007/s00348-016-2140-x.

[44] Bucci, M. A., Cherubini, S., Loiseau, J.-C., and Robinet, J.-C., "Influence of freestream turbulence on the flow over a wall roughness," *Physical Review Fluids*, Vol. 6, No. 6, 2021. https://doi.org/10.1103/physrevfluids.6.063903.

[45] Tempelmann, D., and Hanifi, D., A.and Henningson, "Spatial optimal growth in three-dimensional compressible boundary layers," *Journal of Fluid Mechanics*, Vol. 704, 2012, pp. 251–279. https://doi.org/10.1017/jfm.2012.235.

Downloaded by TU DELFT on January 24, 2023 | http://arc.aiaa.org | DOI: 10.2514/6.2023-2306